

Chemical Science

Accepted Manuscript

This article can be cited before page numbers have been issued, to do this please use: A. K. Mondal, P. Singh Bisht, R. Garg, T. K. Das, N. Bhatt and S. C. Sahoo, *Chem. Sci.*, 2026, DOI: 10.1039/D6SC01358A.



This is an Accepted Manuscript, which has been through the Royal Society of Chemistry peer review process and has been accepted for publication.

Accepted Manuscripts are published online shortly after acceptance, before technical editing, formatting and proof reading. Using this free service, authors can make their results available to the community, in citable form, before we publish the edited article. We will replace this Accepted Manuscript with the edited and formatted Advance Article as soon as it is available.

You can find more information about Accepted Manuscripts in the [Information for Authors](#).

Please note that technical editing may introduce minor changes to the text and/or graphics, which may alter content. The journal's standard [Terms & Conditions](#) and the [Ethical guidelines](#) still apply. In no event shall the Royal Society of Chemistry be held responsible for any errors or omissions in this Accepted Manuscript or any consequences arising from the use of any information it contains.

Chirality Induced Long-Range Spin-Selective Transport in Helical 3D Metal-Organic Frameworks

View Article Online
DOI: 10.1039/C6SC01358A

Pravesh Singh Bisht,^a Rabia Garg,^a Tapan Kumar Das,^b Nidhi Bhatt,^a Subash Chandra Sahoo,^c and Amit Kumar Mondal^{a*}

^a Institute of Nano Science and Technology (INST), Mohali, Sector 81, Sahibzada Ajit Singh Nagar, Punjab 140306, India.

^b Department of Chemical and Biological Physics, Weizmann Institute of Science, Rehovot 7610001, Israel.

^c Department of Chemistry, Panjab University Chandigarh, Sector 14, Chandigarh 160014, India.

Corresponding author email id: amit@inst.ac.in

Abstract:

The exploration of novel chiral molecules as efficient spin-filtering materials via chirality induced spin selectivity (CISS) effect remains an active and evolving area of research within the field of chiral spintronics. Previous studies that evaluated efficient spin filtering materials primarily focused on the degree of spin polarization achieved, often overlooking critical factors such as current intensity and the range of electron conduction. In this work, we endeavoured to provide a balanced assessment of these three parameters, and consequently, we reported highly efficient spin filtering materials based on CISS effect in three-dimensional (3D) chiral metal organic frameworks (MOFs). A significant aspect of this work is the successful demonstration of CISS effect in two homochiral MOF crystals, where we achieved precise control over their high degree of spin-selectivity, a long range of spin filtering ($>1 \mu\text{m}$), and substantial current intensity ($\sim 130 \text{ nA}$). This is attributed to their opposite helical structures and multidimensional electron transport channels. Notably, this study provides the first demonstration of spin-selective transport in transition metal-based helical 3D MOFs. To further validate the spin-dependent transport process in chiral 3D MOFs, we developed a prototype device featuring a spin-valve configuration. Notably, the results obtained from this device correlate well with the



spin-dependent processes and confirm the presence of the CISS effect in the studied MOF materials. Furthermore, we have established a direct correlation between the contact potential difference (CPD) and the chirality of the 3D MOF crystals, offering new insights into their preferential spin transport properties via the CISS effect. This correlation, largely overlooked in previous studies, represents a key advance in understanding and designing efficient CISS-based spintronic materials.

Keywords: Long-range spin filters; Chirality-induced spin selectivity (CISS) effect; Spintronics; Metal organic frameworks (MOFs).

Introduction:

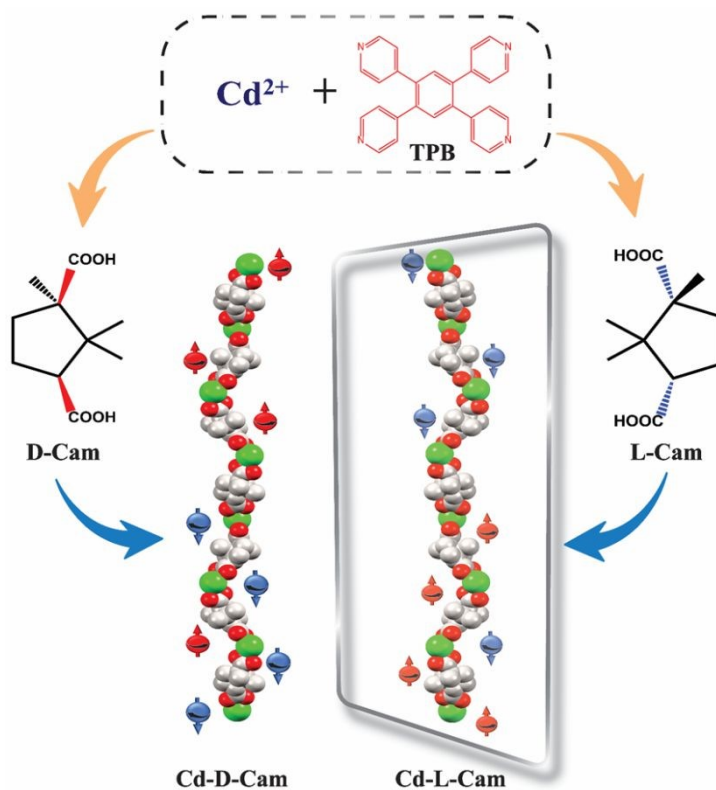
Techniques for generating spin current, as outlined in the literature, are predominantly confined to magnetically active materials and spin-active interfaces.¹ Among these, transition metal ferromagnets and their alloys demonstrate moderate spin polarization (SP) capabilities, thus limiting the spin-dependent effects such as magnetoresistance, spin accumulation, etc.²⁻³ Recently, it has been possible to selectively extract and utilize spin-polarized electrons through the use of chiral compounds. This progress stems from the discovery of chiral-induced spin selectivity (CISS) effect.⁴⁻⁷ Electrons possess an intrinsic quantum mechanical property called spin, which represents their intrinsic angular momentum. It can be viewed as a spinning top having two directions, either clockwise or anticlockwise often referred to as spin up or spin down.⁸ Chirality is the property of asymmetry of a molecule, resulting in the non-superimposable mirror images existence of a molecule known as the enantiomers typically designated as L-form (left-handed) and D-form (right-handed).⁹ When electrons propagate through the helical electrostatic potential of chiral molecules, the spinning motion of electrons gets coupled with its angular momentum via spin-orbit interactions along with the tunnelling mediated charge transport (fundamentally modified by decoherence), thus results in the



preferential transmission of one spin over the other, determined by the handedness of chiral molecule. This phenomenon is therefore referred to as CISS effect and it has gathered renewed interest due to its remarkable ability to control the spin selective electron transmission using chiral materials, that too without the need of an external magnetic field.^{10–17} In light of the rapid developments in this field, a variety of chiral materials such as organic and hybrid systems,^{18,19} organic polymers,^{20–23} MOFs,^{24,25} overcrowded alkenes,^{26,27} and organic-inorganic perovskites,^{28,29} have been engineered for CISS. These materials serve as effective spin filters, successfully addressing challenges such as weak spin-orbit coupling (SOC) and exchange interactions.^{30–32}

Despite significant advancements, the design of chiral materials that enables highly efficient spin polarized electron transport, along with long-range spin transport, remains a key challenge. In this study, we demonstrated that chiral metal-organic frameworks (MOFs) can function as an effective platform for harnessing the CISS effect to enable long range spin-selective electron transport. MOFs are crystalline materials formed from metal ions or clusters linked by organic linkers, that can be one-, two-, or three-dimensional.^{33,34} An important and evolving class of MOF i.e. chiral MOFs are the porous materials having asymmetric structures and are widely used in applications such as chiral transcription, enantiomeric separation, chiral catalysis, and more.^{35,36} The utilization of chiral MOFs for spin selective transport of electrons via the CISS effect is an emerging and underexplored area which is still in its infancy stages. Building on our previous work, which successfully demonstrated spin selectivity in a purely achiral system through the spontaneous resolution technique to obtain random chiral MOF crystals,²⁴ our current objective is to achieve precise control over the spin selectivity as well as long-range spin transport by introducing homochirality in MOFs using chiral building blocks.





Scheme 1: Schematic representation of the studied system and corresponding chirality induced spin dependent electron transfer processes.

Recently, an efficient 3D MOF spin-filter based on paramagnetic Dy^{3+} has been reported by Sebastian *et al.*³⁷ However, the exploration of transition metal-based 3D MOFs within the CISS framework remains largely uncharted. To address this, our current work focuses on the utilization of 3D crystalline MOF as a spin-filtering material, achieved through the self-assembly of the achiral molecule 1,2,4,5-tetra(pyridin-4-yl)benzene (TPB) and chiral camphoric acid (D/L-cam) in the presence of Cd^{2+} ions (Scheme 1). The multidimensional propagation of chiral helices along different crystallographic directions within the MOF may promote multichannel electron transport. Additionally, the significant spin-orbit coupling (SOC) of the 4d transition metal Cd^{2+} centres can enhance the CISS effect. These combined factors likely contribute to the realization of long-range spin-polarized charge transport with high spin polarization (SP) values.

Results and Discussion:



Both the complexes (Cd-D-cam and Cd-L-cam) were synthesized via a solvothermal method involving $\text{Cd}(\text{NO}_3)_2 \cdot 4\text{H}_2\text{O}$, 1,2,4,5-tetra(pyridin-4-yl)benzene (TPB) and D/L-camphoric acid (D/L-cam) in a solvent mixture of DMA and water according to a reported procedure (Fig. S1).³⁸ These crystals have been characterized by the single-crystal X-ray diffraction. The resulting compounds crystallize in a trigonal crystal system with space groups $P3_121$ and $P3_221$, respectively. Each Cd^{2+} ions form a distorted tetrahedral structure by coordinating with two carboxylate groups from D/L-cam and two pyridyl N-atoms of TPB (Fig. 1B, 1F). Only looking at the interaction between Cd^{2+} ions and D/L-cam ligands lead to the formation of a one-dimensional (1D) helical chain of each chiral type along the *c*-axis (Fig. 1D, 1E). The chirality of the camphoric acid ligand (D/L) plays a crucial role in directing the absolute helicity of the chain. The TPB ligand serves as a pivotal linker, connecting four Cd-(D/L)-cam helical chains to construct a sheet-like network along the *bc*-plane, which further vertically extended culminating in a three-dimensional (3D) homochiral framework for each Cd-compound (Fig. 1C, 1H). Although the overall structure is non-interpenetrated, it contains solvent-accessible voids occupied by lattice water molecules and diffused DMA molecules. These diffused DMA molecules could not be accurately assigned, hence masked. The crystallographic data and structural parameters were found consistent with the previous observations³⁸ and were summarized in Tables S1-S2. The corresponding bond lengths and bond angles around the Cd^{2+} are given in Table S2.



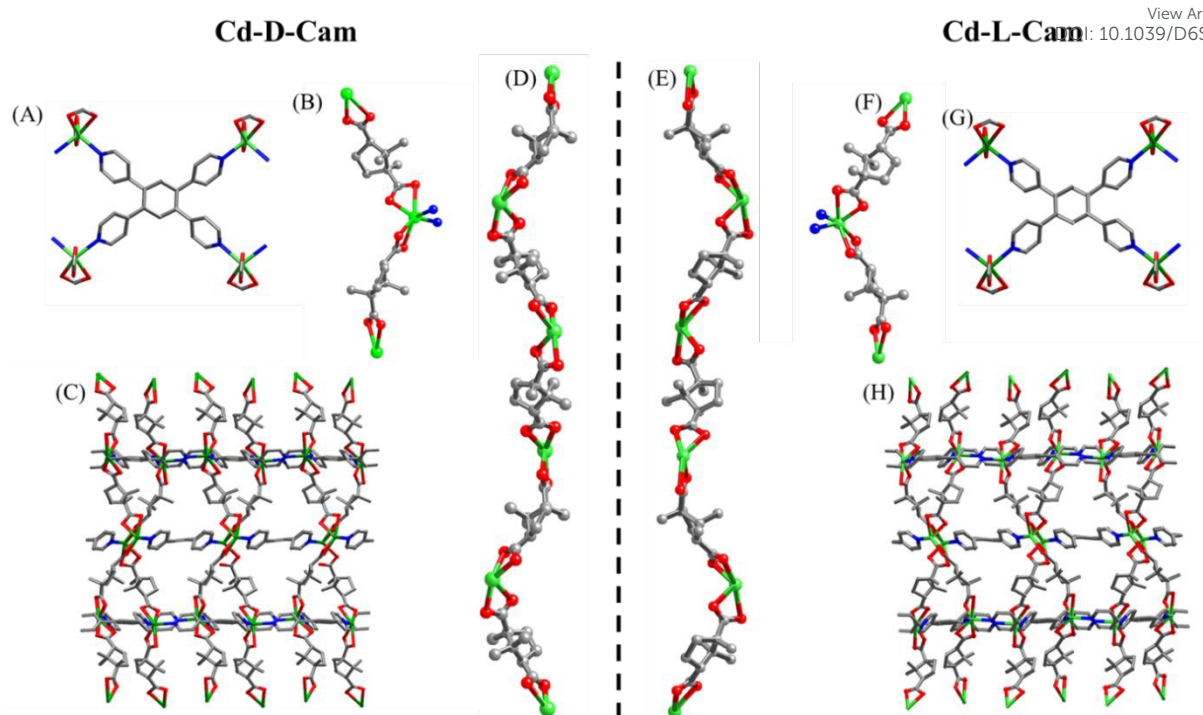


Fig. 1: Structural descriptions of complexes, Cd-D-Cam and Cd-L-Cam. (A, G) The coordination mode of TPB ligands in Cd-D-Cam and Cd-L-Cam. (B, F) The coordination environment of Cd^{2+} ions in Cd-D-Cam and Cd-L-Cam. (C, H) The 3D sheet-like network along the bc -plane in Cd-D-Cam and Cd-L-Cam. (D, E) The 1D helical chains (P and M) consist of Cd^{2+} ions and D/L-cam ligands along the c -axis. Color codes: Cd (green), O (red), N (blue), C (gray).

To evaluate the chiroptical properties of these helical MOFs, UV-vis absorption and circular dichroism (CD) spectra has been recorded (Fig. 2A, 2B). Cd-D-Cam shows a positive cotton effect at around 306 nm and Cd-L-Cam shows an opposite peak at around 305 nm, which confirms their chiral nature. Absorption band at around 305 nm has been observed due to the π - π^* transition of TPB molecules. These results showed that the chirality has been successfully induced in an overall architectural framework of 3D MOF. The high-resolution images of these crystals have been obtained by using scanning electron microscopy (SEM) (Fig. 2C) and atomic force microscopy (AFM) (Fig. 2D). Their elemental analysis has been successfully confirmed by using the energy dispersive X-ray analysis (EDX) (Fig. S2) and X-ray photoelectron spectroscopy (XPS) (Figs. S3-S4).



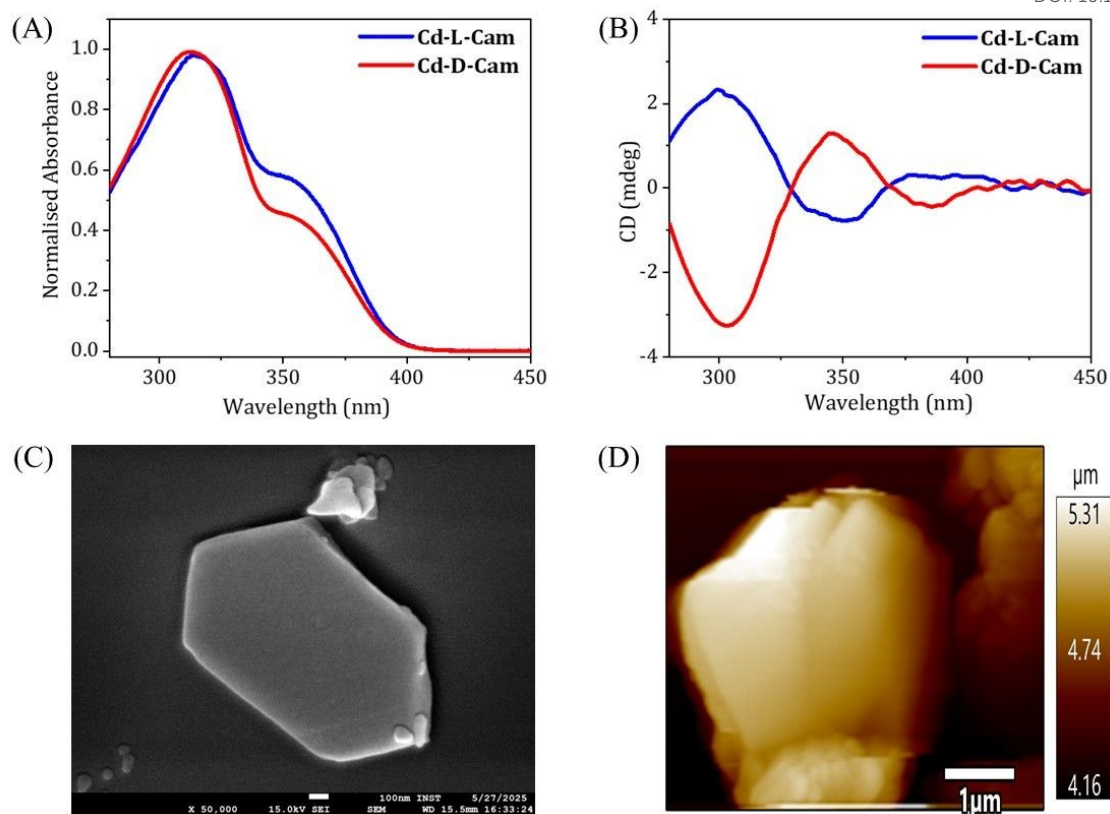


Fig. 2: (A) Absorption spectra of Cd-D-Cam (red) and Cd-L-Cam (blue) crystals. (B) CD spectra of Cd-D-Cam (red) and Cd-L-Cam (blue) showing opposite signals. (C) High-resolution SEM image of a Cd-Cam single crystal. (D) AFM image of Cd-D-Cam crystal having height of ~ 900 nm as shown in height profile image (Fig. S5).

For the spin dependent charge transport measurements in chiral 3D MOFs we have employed the magnetic conducting probe atomic force microscopy (mc-AFM) setup as depicted in Fig. 3A. First, we deposited the crystals onto the gold-coated nickel, Ni/Au (100/8 nm) substrate and the AFM imaging shows the height of crystals at around 800-900 nm (Fig. 2D) and even more than $1\mu\text{m}$ in some cases (Fig. S5). Further, by deploying these crystals for the current versus voltage (I-V) responses under different magnetized condition i.e. magnetic north UP and DOWN condition has been recorded. To control the magnetization direction of Ni layer, a permanent magnet having a magnetic field strength of ~ 0.15 T was placed beneath the ferromagnetic substrate. The measurements were carried in contact mode using a conductive AFM probe with an electrical bias ranging from -2V to $+2\text{V}$ was applied to the substrate. Here,



when electrons are getting transported through the multidimensional helical pathway of a 3D MOF, the chirality of the MOF and the coupling of the electron's angular momentum with its spin came into the effect. During this propagation of electrons through the chiral pathway, spin-orbit coupling along with the tunnelling assisted charge transport (fundamentally modified by decoherence) generates a spin-dependent energy splitting thus favouring transport of one spin orientation over the other depending on the chiral handedness.¹⁷ In case of Cd-D-Cam, there is a constant observation of higher current when substrate was magnetized in UP (green) direction rather than the DOWN (purple) direction (Fig. 3B, S6). Contrarily, for the Cd-L-Cam higher current intensity has been observed when substrate was magnetized in DOWN (purple) direction rather than the UP (green) direction (Fig. 3C, S6). It has been clearly indicated by the slope of the curves that the current intensity transmitted

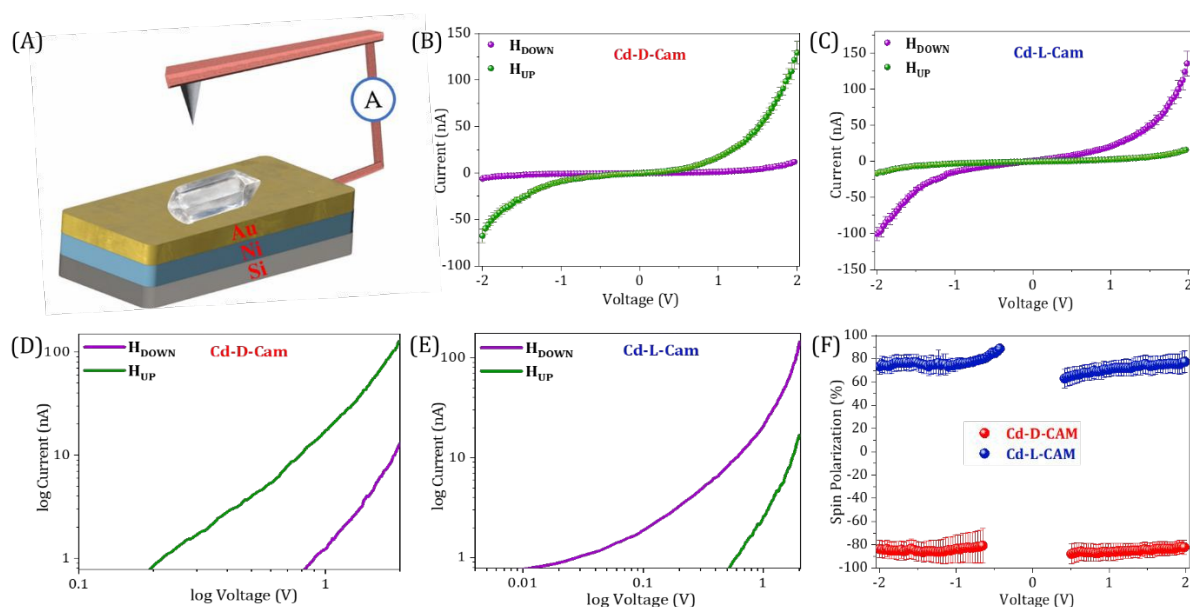


Fig. 3: (A) Schematic representation of the mc-AFM setup used for the spin transport studies of 3D chiral MOFs on Ni/Au (100/8nm). (B, C) The averaged current versus voltage (I-V) curves (with standard error) for Cd-D-Cam and Cd-L-Cam, respectively, with the Ni layer magnetized with the North Pole pointing up (green) or down (purple). (D, E) Corresponding curves as a log-log plot for Cd-D-Cam and Cd-L-Cam crystals, respectively showcasing the different threshold voltages for spin up and spin down injection. (F) Spin polarization as a function of applied bias voltages for Cd-D-CAM (red) and Cd-L-CAM (blue), respectively. The percentage of spin polarization is calculated as $\{(I_{\text{down}} - I_{\text{up}})/(I_{\text{down}} + I_{\text{up}})\} \times 100$. Here, I_{up} and I_{down} are the currents with magnetic north pole up and down, respectively.



through the chiral MOF is highly dependent on the spin polarization direction of the injected electrons, which eventually leads to the chirality induced spin selection phenomena. The spin polarization is expressed by $SP = \{[(I_{\text{down}} - I_{\text{up}})/(I_{\text{down}} + I_{\text{up}})] \times 100\}$, where I_{up} and I_{down} represent the currents at a given potential with magnetic north pole up and down, respectively. For Cd-D-Cam, the calculated spin polarization is 81% while for Cd-L-Cam, the calculated spin polarization is 80% at 2V. From the log plots for Cd-D-Cam, the threshold voltage for down spins exceeds that for up spins (Fig. 3D). Conversely, for Cd-L-Cam, the threshold voltage for up spins exceeds that for down spins (Fig. 3E). It reveals that each spin has a distinct threshold voltage with no evidence of spin flipping during the conduction process therefore holding the significance for the CISS effect even at extremely low voltages. It has to be noted that mc-AFM is a completely localized technique where a very fine cantilever tip with the radius in nanometre scale contacts the sample by making the probe-sample contact area and then recorded the respective I-V curves at different positions. Additionally, we performed the thickness-dependent CISS studies on the single MOF crystals by deliberately choosing crystals of varying thicknesses. Our results demonstrate that the spin filtering efficiency increases consistently with thickness (Fig. S7). The thickness dependence of spin polarization arises from two competing processes: an increase in spin selectivity due to the growing number of chiral barrier layers and spin relaxation effects caused by spin decoherence effects upon diffusion in the chiral layers. As the thickness of the transporting chiral layer increases, the spin polarization rises because electrons have more opportunities to traverse longer distances through chiral potential, thereby enhancing the spin-filtering process. In our studies, we found that the spin polarization increased with thickness up to 800 nm, beyond which it reached saturation. This can be attributed to an increased likelihood of spin dephasing and scattering at greater thicknesses, which can significantly diminish the observed spin selectivity.^{28,39,40}



In prior research, chiral systems have primarily been evaluated for their efficiency as spin-filters based on their spin polarization values. As a result, certain systems have been posed as ideal spin filter, capable of achieving up to 100% spin polarization.³⁷ However, important factors such as current intensity and range of electron conduction pathway have often been overlooked when evaluating the spin-filtering performance. To ensure a more comprehensive evaluation, we should consider spin-polarization (SP) with the corresponding current intensity (I) and conduction range (R) as an important figure of merit (FOM) i.e. $FOM = SP \times I \times R$. To get a physically significant FOM value we have redefined the figure of merit where we have converted both the current and spin conduction range into unitless quantities, so that "figure of merit" will be dimensionless. We express current intensity as I/I^0 and the range of spin filtering as R/R^0 , with I^0 and R^0 standardized at 1 nA and 1 nm, respectively, across all materials for uniform comparison. The updated figure of merit is now defined as $FOM = SP \times I/I^0 \times R/R^0$. From Fig. 4, it is evident that our current 3D helical MOFs exhibit the highest value of FOM, highlighting as exceptionally efficient spin-filtering materials. Data has been extracted only from representative chiral systems measured by mc-AFM measurements. In Table S3 the data table showcases each parameter of the FOM and the value of FOM calculated for each molecular system and we can clearly see the highest value of FOM calculated for our 3D helical MOF system. It is clear that most of the systems attain high spin polarization, while their current intensities are relatively poor. In some cases, particularly in chiral cages⁴¹ and metallo-supramolecules,¹⁹ excellent spin polarization is observed with higher current intensity, although the range of spin conduction pathway is quite shorter than what we have achieved in our work. In our study, we have successfully attained a notable spin polarization (~81%) and high current intensity (>130 nA) with a long-range spin filtering ability (>1 μm). By combining these three parameters, we can therefore assert that our 3D helical MOF system functions as a highly efficient and long-range spin-filter.



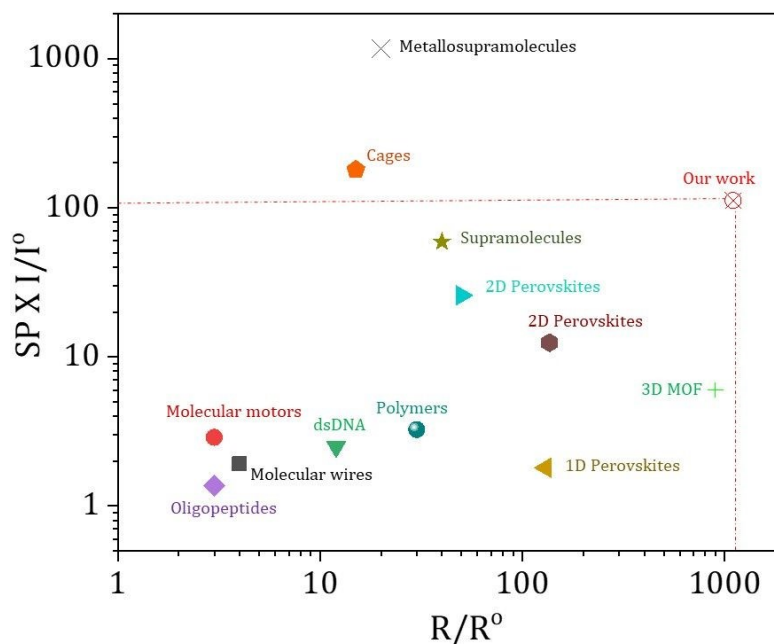


Fig. 4: Representation of spin polarization (SP) with I/I^0 (I is current intensity achieved in nA at the bias voltage of 2V and I^0 is standardised at 1 nA for all systems) against the R/R^0 value (R is the range of spin filtering and R^0 is standardised at 1 nm for all systems). Data has been extracted only from representative chiral systems measured by mc-AFM. Data extracted for 3D MOF, see ref³⁷; 1D perovskites, see ref⁴²; 2D perovskites, see ref^{28,43}; supramolecules, see ref²¹; metallo-supramolecules, see ref¹⁹; chiral cages, see ref⁴¹; polymers, see ref²⁰; peptides and DNA, see ref⁴⁰; molecular motors, see ref²⁶; molecular wires, see ref⁴⁴. Corresponding *FOM* values calculated for all these molecular systems provided in Table S3.

We have further employed Kelvin-probe force microscopy (KPFM) technique to further strengthen the above observations of spin selectivity in chiral 3D MOFs. Here, when charge is getting injected at the interface from ferromagnet to the chiral crystals while altering either the chirality (D/L) or magnetization direction (UP/DOWN), spin-selective interactions at the interface of chiral crystal and the ferromagnetic substrate takes place, where charge polarization is accompanied by the spin-polarization thus leads to the differential charge accumulation at the surface followed by the change in contact potential difference (CPD).^{24,45–}

⁴⁷ In case of Cd-D-Cam, the CPD is 115 mV higher in magnetic UP condition rather than the DOWN condition as seen in Fig. 5A. Conversely, in case of Cd-L-Cam, the CPD is 130 mV higher in magnetic DOWN condition rather than the UP condition (Fig. 5D). It has also been clearly observed from the potential mapping images as well (Fig. 5B-5F) that the CPD



responses are dependent on the chirality of crystals as well as the magnetization direction. The alterations in CPD that arise from the opposite chirality of crystals are related to the penetration of spin-polarized charge from ferromagnet source into chiral framework. This effect is facilitated by the CISS effect, which selectively filters the electrons according to their spin orientation, leveraging the material's chirality.

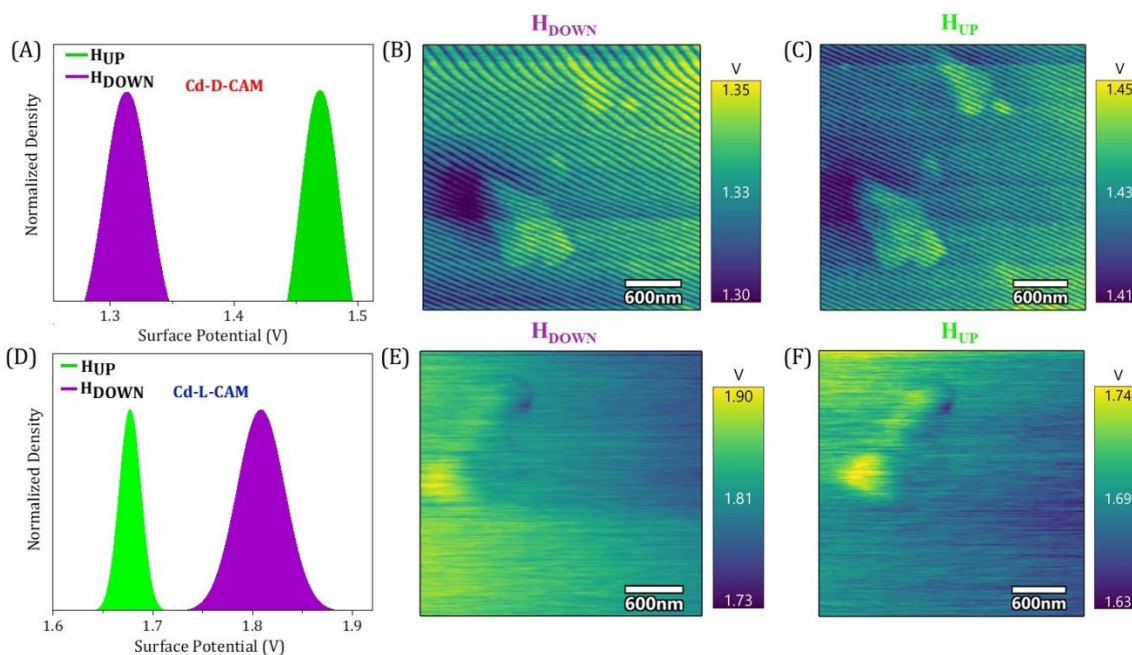


Fig. 5: (A, D) Measured contact potential difference (CPD) distribution are shown for Cd-D-Cam and Cd-L-Cam, respectively, with the ferromagnetic layer magnetized with the north pole pointing up (green) or down (purple). (B, C) Electrostatic potential map of Cd-D-Cam with Ni substrate magnetized with the North Pole pointing down and up orientation, respectively. (E, F) Electrostatic potential map of Cd-L-Cam with Ni substrate magnetized with the North Pole pointing down and up orientation, respectively.

In order to further showcase the role of spin in electron transport process through the chiral MOF materials, we have performed the spin-dependent electrochemical analysis. Similar to the electrochemical setup as used previously,^{48,49} the CV curves were recorded while varying the magnetization direction of a nickel (Ni) substrate as well as changing the chirality of materials. The Ni/Au substrate coated with chiral MOFs act as working electrode, Pt wire used as a counter electrode and for the reference electrode, a 3M KCl saturated Ag/AgCl electrode has



been used. A 1 mM $K_4[Fe(CN)_6]/K_3[Fe(CN)_6]$ (Fe^{2+}/Fe^{3+}) redox couple has been used in current study due to its simple, well-defined redox reaction and well-reported kinetic, electrochemical and thermodynamic parameters. The study was conducted in an aqueous solution at pH 7, using a tris buffer, with the supporting electrolyte of 50 mM NaCl and 50 mM $MgCl_2$. Before the measurements were made, a permanent magnet was placed directly underneath the working electrode and the field strength at the Ni surface was determined to be

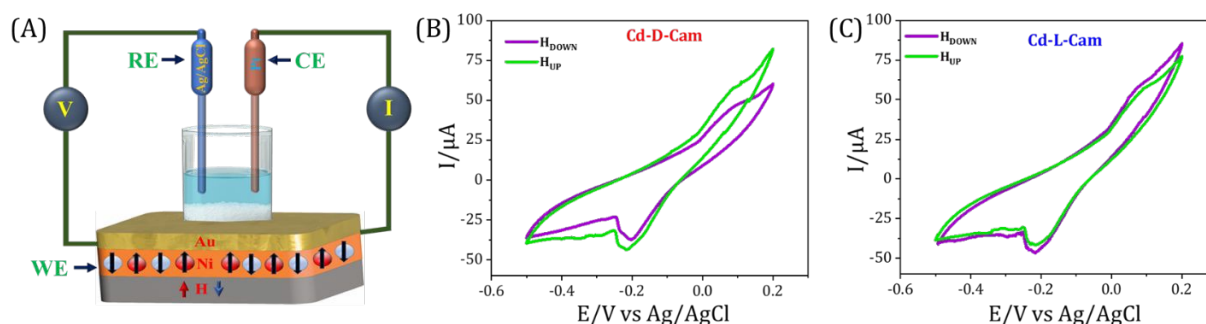


Fig. 6: (A) Spin-dependent electrochemical setup for recording current vs voltage (CV) curve under different magnetization conditions. CV curves of the 1 mM $K_4[Fe(CN)_6]/K_3[Fe(CN)_6]$ redox couple in a pH= 7 (Tris)-buffered, 50 mM NaCl, and 50 mM $MgCl_2$ base electrolyte, aqueous solution: Initial potential = -0.5 V; final potential = $+0.2$ V; scan rate = 50 mV/s. Pt acts as a counter electrode and Ag/AgCl/KCl_{sat} act as a reference electrode. (B, C) CV curves obtained using Cd-D-Cam and Cd-L-Cam, respectively, physisorbed on the Ni/Au working electrode with the Ni layer magnetized with the North Pole pointing UP (green) or DOWN (purple).

0.15 T using a digital Gauss meter. Fig. 6 presents the current versus voltage (I-V) plots for chiral 3D MOFs deposited on Ni under different magnetization direction. The CV curves exhibit a redox behaviour having an oxidation and reduction potential curves at $+0.08$ V and -0.25 V, respectively. The peaks represent the reversible one-electron transfer of the ferrocyanide/ferricyanide couple i.e. $[Fe(CN)_6]^{3-} + e^- \rightleftharpoons [Fe(CN)_6]^{4-}$. Adsorption of microcrystalline film over the substrate alters the charge transfer kinetics as suggested by the increased peak to peak difference and decreased peak current along with the asymmetric nature of anodic and cathodic peak. Such behaviour is generally observed during charge transfer processes through adsorbed molecular films.^{50,51} The CV curves recorded under different magnetic field directions show a clear observation of change in current which indicates that electron transfer through the chiral 3D MOFs is influenced by spin orientation. On applying a



fixed potential for both magnetic conditions, a quantitative comparison of the current values has been done. In case of Cd-D-Cam a higher current value has been observed in magnetic UP condition, while a lower current value has been observed in magnetic DOWN condition (Fig. 6B). Conversely, in case of Cd-L-Cam a higher magnitude of current has been observed in magnetic DOWN condition rather than the magnetic UP condition (Fig. 6C). For the control measurements, we also recorded CV curves for the bare Ni surface in both the magnetic conditions to showcase that the CISS phenomenon arises from the chiral MOF molecules and is independent of the substrate used. It is clearly observed that the obtained CV curves for the bare Ni surface in both the magnetic condition has no observable change in their current values as both the CV curves almost overlap onto each other (Fig. S8). Additionally, it is important to note that the results obtained from spin-dependent electrochemical analysis for two chiral 3D MOFs are consistent with mc-AFM and KPFM studies.

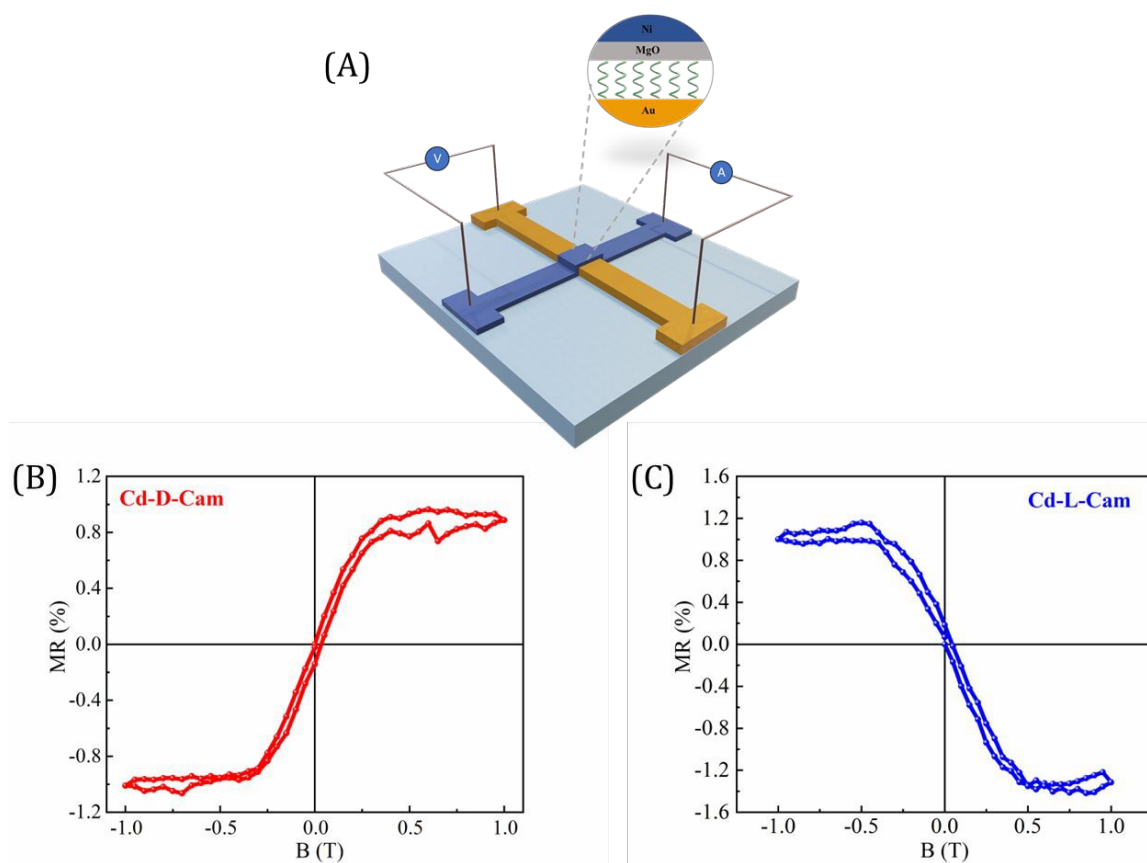


Fig. 7: (A) Schematic representation of the four-probe magnetoresistance (MR) measurement setup with bottom gold and top Ni electrode. (B and C) present the magnetoresistance curves as a function of magnetic field measured with the input current of 0.1 mA at 200 K for Cd-D-Cam and Cd-L-Cam crystals, respectively. MR was measured with the input current of 0.1 mA at 200 K.



Finally, we developed a prototype device in a spin-valve configuration to facilitate the measurement of magnetoresistance (MR) of these chiral MOF crystals. Fig. 7A illustrates the structure of the device, while its crossbar geometry allows for resistance measurements using a standard four-probe configuration. Fig. 7B and 7C present the MR curves as a function of the magnetic field for devices fabricated from Cd-D-Cam and Cd-L-Cam crystals, respectively. The asymmetric MR curve was observed in response to the magnetic field, which was consistent with previous studies on chiral molecules based on the CISS effect.^{27,40} It is important to emphasize that the results obtained from the MR device not only corroborate the presence of the CISS effect in these studied MOF materials but also align closely with the findings from earlier spin-dependent processes as observed in mc-AFM, KPFM, and electrochemical measurements.

Conclusion:

In conclusion, we have successfully demonstrated chirality induced spin-selective transport in 3D MOFs. Our findings indicate that Cd-D-Cam serves as an effective spin filter for up-spin of electrons, while the Cd-L-Cam filters down-spin of electrons. Notably, we achieved a high spin polarization, along with a substantial current intensity and long-range of spin transport. Based on these three key parameters, we present this work as a pioneering contribution to the field. The helicity manifested in different crystallographic directions offers multichannel electron transport, and the Cd²⁺ metal center may play a significant role in the pronounced spin-orbit coupling in the CISS phenomena. Furthermore, our report showcases the CISS effect in 3D chiral MOFs using four different techniques, thereby establishing a robust foundation for their applications as long-range spin filters for room-temperature spintronics devices.

Supporting Information: Materials, methods, synthetic details, sample characterization, and additional measurements are provided in the Supporting Information.



Conflicts of interest: The authors declare no conflict of interest.

View Article Online
DOI: 10.1039/D6SC01358A

Acknowledgements: PSB and RG acknowledge UGC and INST Mohali, respectively for providing fellowships. NB acknowledges DAE-BRNS project for providing fellowship. AKM acknowledges ANRF (Sanction No: ANRF/ECRG/2024/000712/CS) and DAE-BRNS (Sanction No. 58/14/03/2024-BRNS) for financial support. DST-FIST is acknowledged for SCXRD facility at Department of Chemistry, PU, Chandigarh. Authors acknowledge INST Mohali for instrumental support. Authors acknowledge Mr. Krishankant for valuable scientific discussions. All authors have given approval to the final version of the manuscript.

References:

- 1 A. Davidson, V. P. Amin, W. S. Aljuaid, P. M. Haney and X. Fan, *Phys. Lett. A*, 2020, **384**, 126228.
- 2 E. Y. Tsymbal, O. N. Mryasov and P. R. LeClair, *J. Phys.: Condens. Matter*, 2003, **15**, R109.
- 3 K. Takanashi Y. Sakuraba, S. Maekawa, S. O. Valenzuela, E. Saitoh and T. Kimura, *Oxford University Press*, 2012, **5**, 36.
- 4 B. Göhler, V. Hamelbeck, T. Z. Markus, M. Kettner, G. F. Hanne, Z. Vager, R. Naaman and H. Zacharias, *Science*, 2011, **331**, 894–897.
- 5 R. Naaman, Y. Paltiel and D. H. Waldeck, *Nat. Rev. Chem.*, 2019, **3**, 250–260.
- 6 Z. Liu, J. Ai, T. Bai, Y. Fang, K. Ding, Y. Duan, L. Han and S. Che, *Chem*, 2022, **8**, 186–196.
- 7 H. Lu, Z. V. Vardeny and M. C. Beard, *Nat. Rev. Chem.*, 2022, **6**, 470–485.
- 8 R. Naaman, Y. Paltiel and D. H. Waldeck, *Annu. Rev. Biophys.*, 2022, **51**, 99–114.
- 9 R. Matassa, S. C. Ray and Y. Zheng, *Sci. Rep.*, 2024, **14**, 26268.
- 10 B. P. Bloom, Y. Paltiel, R. Naaman and D. H. Waldeck, *Chem. Rev.*, 2024, **124**, 1950–1991.
- 11 R. Naaman, Y. Paltiel and D. H. Waldeck, *J. Phys. Chem. Lett.*, 2020, **11**, 3660–3666.
- 12 R. Naaman and D. H. Waldeck, *J. Phys. Chem. Lett.*, 2012, **3**, 2178–2187.



- 13 R. Gupta, A. Balo, R. Garg, A. K. Mondal, K. B. Ghosh and P. C. Mondal, *Chem. Sci.*, 2024, **15**, 18751–18771. Article Online
DOI: 10.1039/D3SC01358A
- 14 C. D. Aiello, J. M. Abendroth, M. Abbas, A. Afanasev, S. Agarwal, A. S. Banerjee, D. N. Beratan, J. N. Belling, B. Berche, A. Botana, J. R. Caram, G. L. Celardo, G. Cuniberti, A. Garcia-Etxarri, A. Dianat, I. Diez-Perez, Y. Guo, R. Gutierrez, C. Herrmann, J. Hihath, S. Kale, P. Kurian, Y.-C. Lai, T. Liu, A. Lopez, E. Medina, V. Mujica, R. Naaman, M. Noormandipour, J. L. Palma, Y. Paltiel, W. Petuskey, J. C. Ribeiro-Silva, J. J. Saenz, E. J. G. Santos, M. Solyanik-Gorgone, V. J. Sorger, D. M. Stemer, J. M. Ugalde, A. Valdes-Curiel, S. Varela, D. H. Waldeck, M. R. Wasielewski, P. S. Weiss, H. Zacharias and Q. H. Wang, *ACS Nano*, 2022, **16**, 4989–5035.
- 15 S. Firouzeh, S. Illescas-Lopez, M. A. Hossain, J. M. Cuerva, L. Álvarez de Cienfuegos and S. Pramanik, *J. Chem. Phys.*, 2023, **159**, 034708.
- 16 S. Mishra, S. Pirbadian, A. K. Mondal, M. Y. El-Naggar and R. Naaman, *J. Am. Chem. Soc.*, 2019, **141**, 19198–19202.
- 17 M. Mena, S. Varela, B. Berche and E. Medina, *J. Stat. Mech.*, 2024, 084001.
- 18 A. Carella, S. Mishra, C. Ferrari, D. Vanossi, F. Rossella, F. Pop, N. Avarvari, H. Htoon, J. A. Hollingsworth, E. G. Bowes, S. Majumder, A. C. Jones and C. Fontanesi, *Nanoscale*, 2025, **17**, 2599–2607.
- 19 R. Garg, P. S. Bisht, N. Bhatt, N. Nakka and A. K. Mondal, *Chem. Mater.*, 2025, **37**, 6293–6301.
- 20 A. K. Mondal, M. D. Preuss, M. L. Ślęczkowski, T. K. Das, G. Vantomme, E. W. Meijer and R. Naaman, *J. Am. Chem. Soc.*, 2021, **143**, 7189–7195.
- 21 P. S. Bisht, R. Garg, N. Nakka and A. K. Mondal, *J. Phys. Chem. Lett.*, 2024, **15**, 6605–6610.
- 22 N. Nakka, R. Garg, P. S. Bisht and A. K. Mondal, *Small*, 2024, **20**, 2405691.



- 23 S. Firouzeh, S. Illescas-Lopez, M. A. Hossain, J. M. Cuerva, L. Álvarez de Cienfuegos and S. Pramanik, *ACS Nano*, 2023, **17**, 20424–20433. View Article Online
DOI: 10.1039/D3SC01358A
- 24 R. Garg, P. S. Bisht, S. C. Sahoo and A. K. Mondal, *Angew. Chem. Int. Ed.*, 2024, **64**, e202418222.
- 25 A. K. Mondal, N. Brown, S. Mishra, P. Makam, D. Wing, S. Gilead, Y. Wiesenfeld, G. Leitus, L. J. W. Shimon, R. Carmieli, D. Ehre, G. Kamieniarz, J. Fransson, O. Hod, L. Kronik, E. Gazit and R. Naaman, *ACS Nano*, 2020, **14**, 16624–16633.
- 26 Q. Zhu, W. Danowski, A. K. Mondal, F. Tassinari, C. L. F. van Beek, G. H. Heideman, K. Santra, S. R. Cohen, B. L. Feringa and R. Naaman, *Adv. Sci.*, 2021, **8**, 2101773.
- 27 M. Suda, Y. Thathong, V. Promarak, H. Kojima, M. Nakamura, T. Shiraogawa, M. Ehara and H. M. Yamamoto, *Nat. commun.*, 2019, **10**, 2455.
- 28 H. Lu, J. Wang, C. Xiao, X. Pan, X. Chen, R. Brunecky, J. J. Berry, K. Zhu, M. C. Beard and Z. V. Vardeny, *Sci. Adv.*, 2019, **5**, eaay0571.
- 29 Y.-H. Kim, Y. Zhai, H. Lu, X. Pan, C. Xiao, E. A. Gaulding, S. P. Harvey, J. J. Berry, Z. V. Vardeny, J. M. Luther and M. C. Beard, *Science*, 2021, **371**, 1129–1133.
- 30 Q. Qian, H. Ren, J. Zhou, Z. Wan, J. Zhou, X. Yan, J. Cai, P. Wang, B. Li, Z. Sofer, B. Li, X. Duan, X. Pan, Y. Huang and X. Duan, *Nature*, 2022, **606**, 902–908.
- 31 V. A. Dediu, L. E. Hueso, I. Bergenti and C. Taliani, *Nat. Mater.*, 2009, **8**, 707–716.
- 32 J.-W. Yoo, C.-Y. Chen, H. W. Jang, C. W. Bark, V. N. Prigodin, C. B. Eom and A. J. Epstein, *Nat. Mater.*, 2010, **9**, 638–642.
- 33 V. F. Yusuf, N. I. Malek and S. K. Kailasa, *ACS Omega*, 2022, **7**, 44507–44531.
- 34 Y. Li, G. Wen, J. Li, Q. Li, H. Zhang, B. Tao and J. Zhang, *Chem. Commun.*, 2022, **58**, 11488–11506.
- 35 W. Gong, Z. Chen, J. Dong, Y. Liu and Y. Cui, *Chem. Rev.*, 2022, **122**, 9078–9144.



- 36 M. Ma, J. Chen, H. Liu, Z. Huang, F. Huang, Q. Li and Y. Xu, *Nanoscale*, 2022, **14**, 13405–13427. View Article Online
DOI: 10.1039/D2SC01358A
- 37 U. Huizi-Rayo, J. Gutierrez, J. M. Seco, V. Mujica, I. Diez-Perez, J. M. Ugalde, A. Tercjak, J. Cepeda and E. San Sebastian, *Nano Lett.*, 2020, **20**, 8476–8482.
- 38 P.-F. Gao, Y.-Y. Jiang, H. Liu, M.-S. Zhou, T. Li, H.-R. Fu, L.-F. Ma and D.-S. Li, *ACS Appl. Mater. Interfaces*, 2022, **14**, 16435–16444.
- 39 D. K. Bhowmick, T. K. Das, K. Santra, A. K. Mondal, F. Tassinari, R. Schwarz, C. E. Diesendruck and R. Naaman, *Sci. Adv.*, 2022, **8**, eabq2727.
- 40 S. Mishra, A. K. Mondal, S. Pal, T. K. Das, E. Z. B. Smolinsky, G. Siligardi and R. Naaman, *J. Phys. Chem. C*, 2020, **124**, 10776–10782.
- 41 Y. Wang, Y. Zhang, Y.-Y. Wang and Q. Yan, *J. Am. Chem. Soc.*, 2025, **147**, 8751–8759.
- 42 Y. Lu, Q. Wang, R. Chen, L. Qiao, F. Zhou, X. Yang, D. Wang, H. Cao, W. He, F. Pan, Z. Yang and C. Song, *Adv. Funct. Mater.*, 2021, **31**, 2104605.
- 43 S. Dan, S. Paramanik and A. J. Pal, *ACS Nano*, 2024, **18**, 35644–35653.
- 44 C. H. Ko, Q. Zhu, F. Tassinari, G. Bullard, P. Zhang, D. N. Beratan, R. Naaman and M. J. Therien, *Proc. Natl. Acad. Sci. USA*, 2022, **119**, e2116180119.
- 45 P. M. Theiler, C. Ritz, R. Hofmann and A. Stemmer, *Nano Lett.*, 2023, **23**, 8280–8287.
- 46 S. Ghosh, S. Mishra, E. Avigad, B. P. Bloom, L. T. Baczewski, S. Yochelis, Y. Paltiel, R. Naaman and D. H. Waldeck, *J. Phys. Chem. Lett.*, 2020, **11**, 1550–1557.
- 47 R. Naaman, Y. Paltiel and D. H. Waldeck, *J. Phys. Chem. Lett.*, 2020, **11**, 3660–3666.
- 48 M. Kettner, B. Göhler, H. Zacharias, D. Mishra, V. Kiran, R. Naaman, D. H. Waldeck, S. Şek, J. Pawłowski and J. Juhaniewicz, *J. Phys. Chem. C*, 2015, **119**, 14542–14547.
- 49 P. C. Mondal, N. Kantor-Uriel, S. P. Mathew, F. Tassinari, C. Fontanesi and R. Naaman, *Adv. Mater.*, 2015, **27**, 1924–1927.



- 50 D. Mishra, T. Z. Markus, R. Naaman, M. Kettner, B. Göhler, H. Zacharias, N. Friedman, M. Sheves and C. Fontanesi, *Proc. Natl. Acad. Sci. USA*, 2013, **110**, 14872–14876. View Article Online
DOI: 10.1039/C3SC01358A
- 51 B. Liu, A. J. Bard, M. V. Mirkin and S. E. Creager, *J. Am. Chem. Soc.*, 2004, **126**, 1485–1492.



The data supports the article are provided in the supporting information file.

